Critical Role of Acceptor Dopants in Designing Highly Stable and Compatible Proton-Conducting Electrolytes for Reversible Solid Oxide Cells

Journal:	*Energy & Environmental Science*
Manuscript ID	EE-ART-04-2022-001104.R1
Article Type:	Paper
Date Submitted by the Author:	09-May-2022
Complete List of Authors:	Luo, Zheyu; Georgia Institute of Technology, Materials Science and Engineering Zhou, Yucun; Georgia Institute of Technology, School of Materials Science and Engineering Hu, Xueyu; Georgia Institute of Technology, School of Materials Science and Engineering Kane, Nicholas; Georgia Institute of Technology, School of Materials Science and Engineering Li, Tongtong; Georgia Institute of Technology Zhang, Weilin; Georgia Institute of Technology, School of Materials Science and Engineering Liu, Zhijun; Georgia Institute of Technology, Materials Science and Engineering ding, yong; Georgia Institute of Technology Liu, Ying; Phillips 66 Company Liu, Meilin; Georgia Institute of Technology, School of Materials Science and Engineering

SCHOLARONE™
Manuscripts

ARTICLE

Critical Role of Acceptor Dopants in Designing Highly Stable and Compatible Proton-Conducting Electrolytes for Reversible Solid Oxide Cells

Zheyu Luo, ‡[a] Yucun Zhou, ‡[a] Xueyu Hu,[a] Nichloas Kane,[a] Tongtong Li,[a] Weilin Zhang,[a] Zhijun Liu,[a] Yong Ding,[a] Ying Liu,[b] and Meilin Liu [*a]

Proton-conducting electrolytes are receiving increasing attention due to their high ionic conductivity at intermediate temperatures, enabling the operation of solid oxide cells with high energy efficiency at low cost. However, the effect of B-site dopants on the properties of doped barium hafnate-cerate electrolyte materials, especially in single cells under operating conditions, has not been systematically studied. Here we report our findings in the development of a series of proton-conducting electrolytes with a general formula of $BaHf_{0.1}Ce_{0.7}R_{0.2}O_{3-\delta}$ (BHCR172, R = Yb, Er, Y, Gd, Sm). The results reveal that electrical conductivity, ionic transference number, chemical stability against steam and CO_2, and compatibility with NiO during sintering are all closely correlated with the dopant size. In particular, the reaction with NiO is found to strongly affect the properties of the electrolytes and hence cell performance. Among all tested compositions, $BaHf_{0.1}Ce_{0.7}Yb_{0.2}O_{3-\delta}$ (BHCYb172) shows excellent chemical stability and minimal reactivity towards NiO, as predicted from density functional theory (DFT)-based calculations and confirmed by experimental results. In addition, proton-conducting reversible solid oxide cells (P-ReSOCs) based on the optimized electrolyte composition, BHCYb172, demonstrate exceptional performance and stability, achieving a remarkable peak power density of 1.74 W cm^{-2} (O_2 as the oxidant) at 600 ^{o}C in the fuel cell mode and a high current density of 2.0 A cm^{-2} at 1.3 V and 600 ^{o}C in the steam electrolysis mode while maintaining excellent durability for over 1000 h.

Broader context

While impressive advances are being made in enhancing the efficiency while reducing the cost of renewable energy technologies (e.g., solar & wind), the integration of them with the existing electric grids is hindered by the lack of efficient and cost-effective energy storage technologies. Reversible solid oxide cells (ReSOCs) that allow efficient conversion between chemical fuels and electrical energy are a promising option for large scale energy storage and load leveling. In particular, ReSOCs based on proton conductors (P-ReSOCs) have potential for efficient operation at intermediate temperatures (400 - 650 ^{o}C), which greatly reduces the cost while prolonging the operational life. However, the widespread application of P-ReSOCs hinges on the development of highly conductive and durable proton conductors. Here we report a new proton-conducting electrolyte, $BaHf_{0.1}Ce_{0.7}Yb_{0.2}O_{3-\delta}$ (BHCYb172), with high proton conductivity, good compatibility with a Ni-based fuel electrode during fabrication, and excellent chemical stability under operating conditions in both the fuel cell and electrolysis modes. The remarkable enhancement in properties of the electrolyte is attributed mainly to rational selection of proper dopants. The concept may offer insights into rational design of novel materials for other chemical and energy transformation technologies, including metal-air batteries, electrolyzers, and electrocatalysis.

Introduction

Climate change is one of the urgent challenges facing us today, and the development of clean, secure, and sustainable energy is a top priority within the scientific community. H_2 is one of the many renewable energy sources that have the potential to replace fossil fuels in order to cut CO_2 emissions and achieve carbon neutrality.[1, 2] Reversible solid oxide cells (ReSOCs), which can operate efficiently under both fuel cell (H_2 to electricity) and electrolysis (electricity to H_2) modes in a switchable manner, are a game changer for the implementation of renewable (e.g., solar, wind, and geothermal) energy technologies because they can bridge the gap between where or when electricity is generated and where or when it is actually needed. For example, ReSOCs can be used as an electrolyzer to produce H_2 (or other clean chemical fuels) when extra electricity is available from wind turbines or solar cells in remote locations; when electricity is needed during night, they can be run as a fuel cell to convert H_2 to electricity. ReSOCs are ideally suited for load leveling to bridge the gap between production and use of electricity on a large scale.

[a.] School of Materials Science and Engineering, Georgia Institute of Technology, Atlanta, GA 30332-0245, USA. Email: meilin.liu@mse.gatech.edu
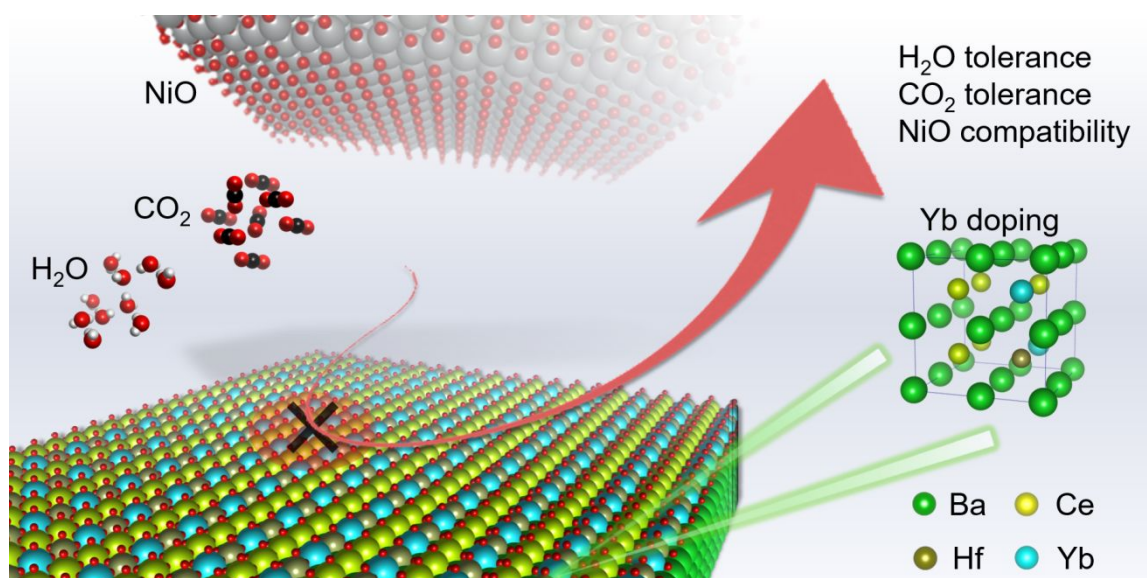[b.] Phillips 66 Company, 2331 CityWest Blvd, Houston, TX, 77042, USA

Fig. 1 Schematic of the properties of BHCYb172.

Both oxygen ion-conducting and proton-conducting electrolytes have been used for ReSOCs.[3] The ReSOCs based on proton-conducting electrolytes are attracting more attention in recent years since the electrolytes can achieve a much higher ionic conductivity (e.g., 0.01 S cm^{-2} at 500 °C) than the conventional oxide ion-conducting counterparts at intermediate temperatures, enabling the application of low-cost cell components. Moreover, water is formed/provided on the air electrode side of the cell, effectively preventing fuel dilution and nickel oxidation problems associated with oxide ion conductor-based cells.[4-7] Accordingly, proton conductor-based ReSOCs have great potential to achieve high efficiency at low cost. However, one of the reasons that they have not been widely adopted is the difficulty in finding an electrolyte material that possesses both high ionic conductivity and sufficient stability against high concentrations of steam and carbon dioxide.[8, 9]

To date, doped barium cerates, doped barium zirconates, and their solid solutions are the most widely used proton-conducting electrolytes.[10-15] Research focus has gradually shifted from zirconates to cerates due to enhanced conductivity and favorable sinterability.[16-21] Undoped barium zirconates or cerates have limited conductivity because proton conduction requires the creation of protonic defects in the ABO_3 perovskite lattice through dissociative adsorption of water (Reaction 1). In order to obtain sufficient proton conductivity under humidified conditions, it is necessary to introduce extrinsic oxygen vacancies by doping to allow for the incorporation of water, and acceptor-doping is the most commonly adopted strategy. For example, replacing two cerium ions by two yttrium ions will produce one oxygen vacancy (Reaction 2). Subsequently, the oxygen vacancy can accommodate a water molecule to produce protonic charge carriers; the motion of these protons contributes to ionic conduction.[22-24] Theoretically, proton conductivity depends on both the concentration and mobility of the protonic charge carriers. Although all trivalent dopants are

likely going to introduce similar amounts of oxygen vacancies if they can be successfully doped into the B-site of the perovskite, not all of them participate in the hydration reaction.[25] For protonated charge carriers, their mobility within the material lattice also depends sensitively on the choice of dopants, since the degree of the proton trapping effect varies greatly as the constituent ions change.[26, 27] To date, many trivalent elements have been tried as dopants in the barium cerate family and reasonable electrochemical performance has been demonstrated.[28, 29] However, detailed correlations between the choice of dopant and the electrochemical properties of the electrolyte have not been systematically explored, especially in single cells under operating conditions, which hinders the rational design and optimization of ReSOCs.

In this work, we have systematically investigated a series of proton-conducting electrolytes with a general formula of $BaHf_{0.1}Ce_{0.7}R_{0.2}O_{3-\delta}$ (BHCR172, R = Yb, Er, Y, Gd, Sm) to uncover the correlations between R^{3+} and electrical conductivity, ionic transference number, chemical stability, compatibility with NiO, and cell performance.[30] It is found that both conductivity and chemical stability are strongly correlated with dopant size, and NiO compatibility increases as the ionic radius of the rare earth dopant decreases. Moreover, reactivity with NiO during sintering is identified as another critical parameter that determines the performance on the single cell level. A Yb-doped electrolyte, $BaHf_{0.1}Ce_{0.7}Yb_{0.2}O_{3-\delta}$ (BHCYb172), offers excellent chemical stability against both H_2O and CO_2 and the best electrode compatibility when compared to other compositions, as confirmed by both experimental and computational results (Fig. 1). Further, proton-conducting reversible solid oxide cells (P-ReSOCs) based on the BHCYb172 electrolyte were fabricated and tested under typical operating conditions, demonstrating exceptional performance and stability in both fuel cell and electrolysis modes.
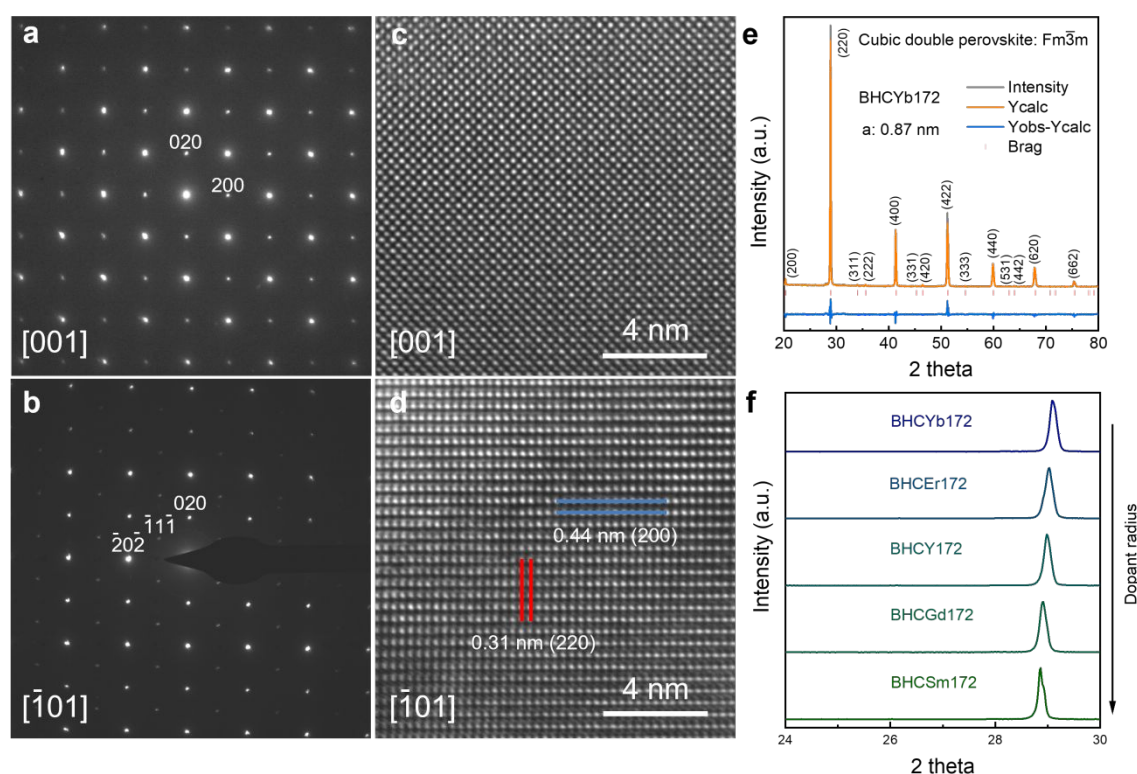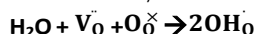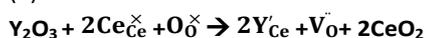
Fig. 2 SAED patterns of BHCYb172 along the a) [001] and b) [$\bar{1}$01] zone axis aligned parallel to the electron beam. HRTEM images corresponding to the c) [100] and d) [$\bar{1}$01] zone axis of the sample. e) XRD Rietveld refinement for BHCYb172. f) Magnified view of the (220) peak of BHCR172 (R = Yb, Er, Y, Gd, Sm).

$$H_2O + V_O^{\cdot\cdot} + O_O^{\times} \rightarrow 2OH_O^{\cdot}$$

(1)

$$Y_2O_3 + 2Ce_{Ce}^{\times} + O_O^{\times} \rightarrow 2Y_{Ce}' + V_O^{\cdot\cdot} + 2CeO_2$$

(2)

Results and discussion

Structural characterization of BHCR172

The crystal structures of Yb/Er/Y/Gd/Sm-doped BHCR172 and BaZr$_{0.1}$Ce$_{0.7}$Y$_{0.1}$Yb$_{0.1}$O$_{3-\delta}$ (BZCYYb1711) were investigated using X-Ray diffraction (XRD). As shown in Fig. S1 (ESI), all as-sintered samples have a cubic perovskite structure. To gain a deeper understanding of the structural arrangement, selected area electron diffraction (SAED) patterns and high-resolution transmission electron microscope (HRTEM) images were collected for BHCYb172 (Fig. 2a-d, Fig. S2, ESI). The SAED patterns can be successfully indexed according to the cubic double perovskite structure with a space group of Fm$\bar{3}$m. The SAED pattern of BHCYb172 is characteristic of a typical cubic perovskite lattice along the [001] zone axis of the sample aligned parallel to the electron beam. In addition to the Bragg reflections characteristic of the cubic perovskite unit cell, superlattice reflections/existence of the ($\bar{1}1\bar{1}$) planes were observed along the [$\bar{1}$01] zone axis of the sample, indicating the presence of a double perovskite lattice, which is attributed to B-site cation ordering in the structure.[31] In the case of BHCYb172, the ordering is mainly caused by the differences in ionic radius and charges among the Hf^{4+}, Ce^{4+}, and Yb^{3+} ions. The ordered dopant structures could be beneficial to proton conductivity

through a possible lower dimensional proton conduction pathway in which enabled by a percolated dopant network.[32, 33] A distance of 0.44 nm between characteristic rows of (200) are observed, and the corresponding lattice parameter for a Fm$\bar{3}$m double perovskite unit cell should be 2*0.44 nm=0.88 nm, which is consistent with the lattice parameter obtained from XRD Rietveld refinement (Fig. 2e).

Fig. S3 (ESI) shows the crystal structure of BHCYb172 with a Fm$\bar{3}$m space group, in which some of the B-sites (4a) are occupied by ordered Ce^{4+}, whereas the remaining Ce^{4+}, Hf^{4+}, and Yb^{3+} are situated in the 4b-site. Fig. 2f shows a magnified view of the (220) peak of BHCR172 (R = Yb, Er, Y, Gd, Sm). As the ionic radius of R increases, the peak positions shift to lower angles, which indicates an increase in the lattice parameter and cell volume, confirming the desired materials were obtained.

Investigation into the electrochemical properties of acceptor-doped electrolytes

The conductivities of dense BHCR172 (R = Yb, Er, Y, Gd, Sm) electrolyte pellets were measured in argon with 3% H$_2$O using electrochemical impedance spectrometry (EIS) at temperatures ranging from 400 to 700 °C (Fig. S4, ESI). From the example Nyquist plots of the EIS scans for BHCYb172, only one clear intercept on the x-axis is observed, and the grain and grain boundary contributions cannot be separated at all temperatures (Fig. S5, ESI). As shown in Fig. 3a, conductivities of BHCR172 electrolytes are comparable to the state-of-the-art proton-conducting electrolyte BZCYYb1711, and all tested
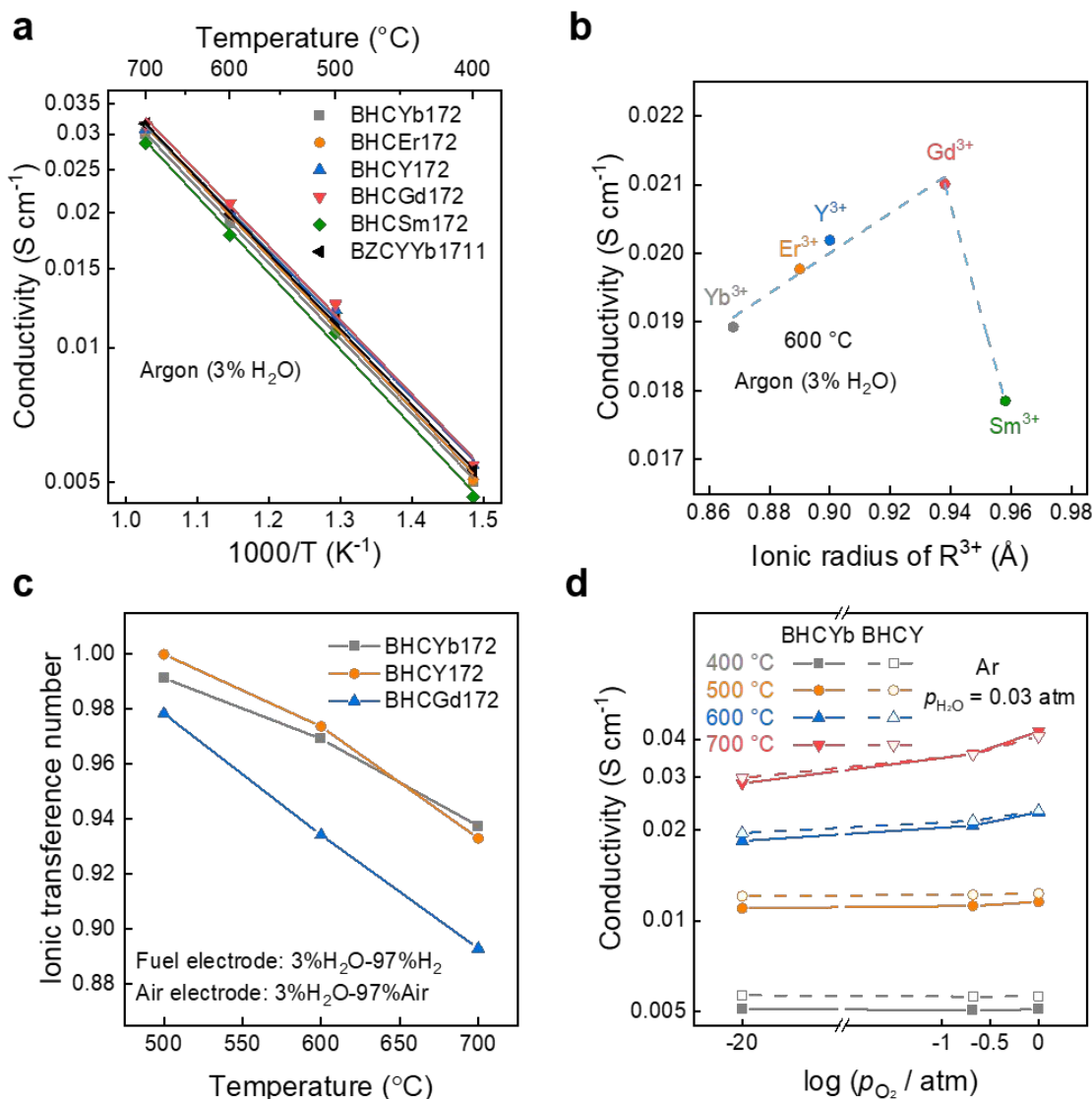
Fig. 3 a) Conductivity of BHCR172 (R = Yb, Er, Y, Gd, Sm) and BZCYYb1711 as a function of temperature. b) Conductivity of BHCR172 at 600 °C as a function of ionic radius of R^{3+}. c) Ionic transference number measured under cell operation conditions. d) Conductivity of BHCYb and BHCY172 as a function of po_2 at different temperatures.

compositions showed a low activation energy in range of 0.32-0.34 eV, which is characteristic for proton conductors.[34] The conductivity at 600 °C as a function of dopant size shows a gradual increase from Yb^{3+} to Gd^{3+}, followed by an abrupt drop once the dopant size is further increased to 0.958 nm for Sm^{3+} (Fig. 3b). As discussed by Amsif et al., proton conduction in perovskite oxides is favored by minimal deviation from the ideal cubic structure and maximal lattice free volume. Since both the lattice distortion and free volume of perovskite oxides increase as the ionic radius of the rare earth dopant gets larger, trivalent dopants with an intermediate ionic radius are expected to give the highest conductivity as they offer balanced lattice distortion and free volume, which might explain the optimized conductivity of Gd-doped sample.[35] Another possibility is the partial substitution of large Sm^{3+} cations on the Ba-site, which would result in the consumption of oxygen vacancies, decreasing overall conductivity, while smaller cations can only situate at the B-site.[36]

As EIS only gives total electrical conductivity, the ionic transference number, t_{ion}, was measured to determine the actual ionic contribution to electrical conduction in the materials under realistic cell operating conditions.[37] As shown in Fig. 3c, the measured t_{ion} is close to unity at 500 °C for all materials and decreases with increasing temperature, suggesting that ionic species are the only mobile charge carries at temperatures lower than or close to 500 °C. It is reported that $BaCeO_3$-based proton conductors are nearly pure ionic conductors under reducing atmospheres, but electronic leakage could be a concern under oxidizing atmospheres (i.e., high partial pressure of oxygen, po_2), in which O_2 can combine with oxygen vacancies inside the material to form electron holes, leading to electronic leakage (Reaction 3).[38-40] This reaction is more favorable at temperatures higher than 600 °C as dehydration becomes significant. Without enough water to interact with oxygen vacancies to generate protonic defects, the oxygen vacancy defects can freely combine with O_2 to

produce electron holes, resulting in observable electronic leakage at elevated temperatures.[41-43] The results from ionic transference number measurements are consistent with the observed dependence of conductivity on po_2. While po_2 has little effect on the total electrical conductivity at 400 and 500 °C, a clear increase in conductivity with po_2 is observed at 600 and 700 °C, due likely to the increased contribution from electron holes (Fig. 3d and Fig. S6, ESI).

It has been reported that the ionic transference number decreases with increasing ionic radius of the trivalent dopant.[44] Thus, although $BaHf_{0.1}Ce_{0.7}Gd_{0.2}O_{3-\delta}$ (BHCGd172) shows the highest conductivity from EIS measurements, the larger electronic contribution to the conductivity makes it less suitable for ReSOCs. In contrast, both Y- and Yb-doped samples possess highly desirable ionic transference numbers ($t_{ion} > 97\%$ at 600 °C), making them better candidates as electrolyte materials for ReSOCs.

$$O_2 + 2V_O^{\cdot\cdot} \rightarrow 4h^{\cdot} + 2O_O^{\times}$$

(3)
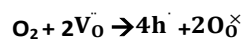
Impact of acceptor dopants on the chemical stability against H_2O and CO_2

It is reported that acceptor-doped barium cerate materials are vulnerable to high concentrations of steam and carbon dioxide with the formation of $Ba(OH)_2$ and $BaCO_3$, respectively.[45-48] The stability of various BHCR172 compositions were tested in CO_2 conditions as the formation of $BaCO_3$ can easily be detected using conventional characterization techniques such as XRD, while the solubility of the $Ba(OH)_2$ impurity phase in water prevents its identification by various characterization techniques. To test the stability of these materials, XRD patterns were obtained after exposing electrolyte pellets to 30% CO_2 (3% H_2O) in Ar for 50 h at 500 °C. As shown in Fig. S7a-b (ESI), the degradation phase was identified as $BaCO_3$ by XRD. To quantify the extent of degradation, the ratio of the $BaCO_3$ peak intensity to that of the original perovskite (at around 29°) was calculated,
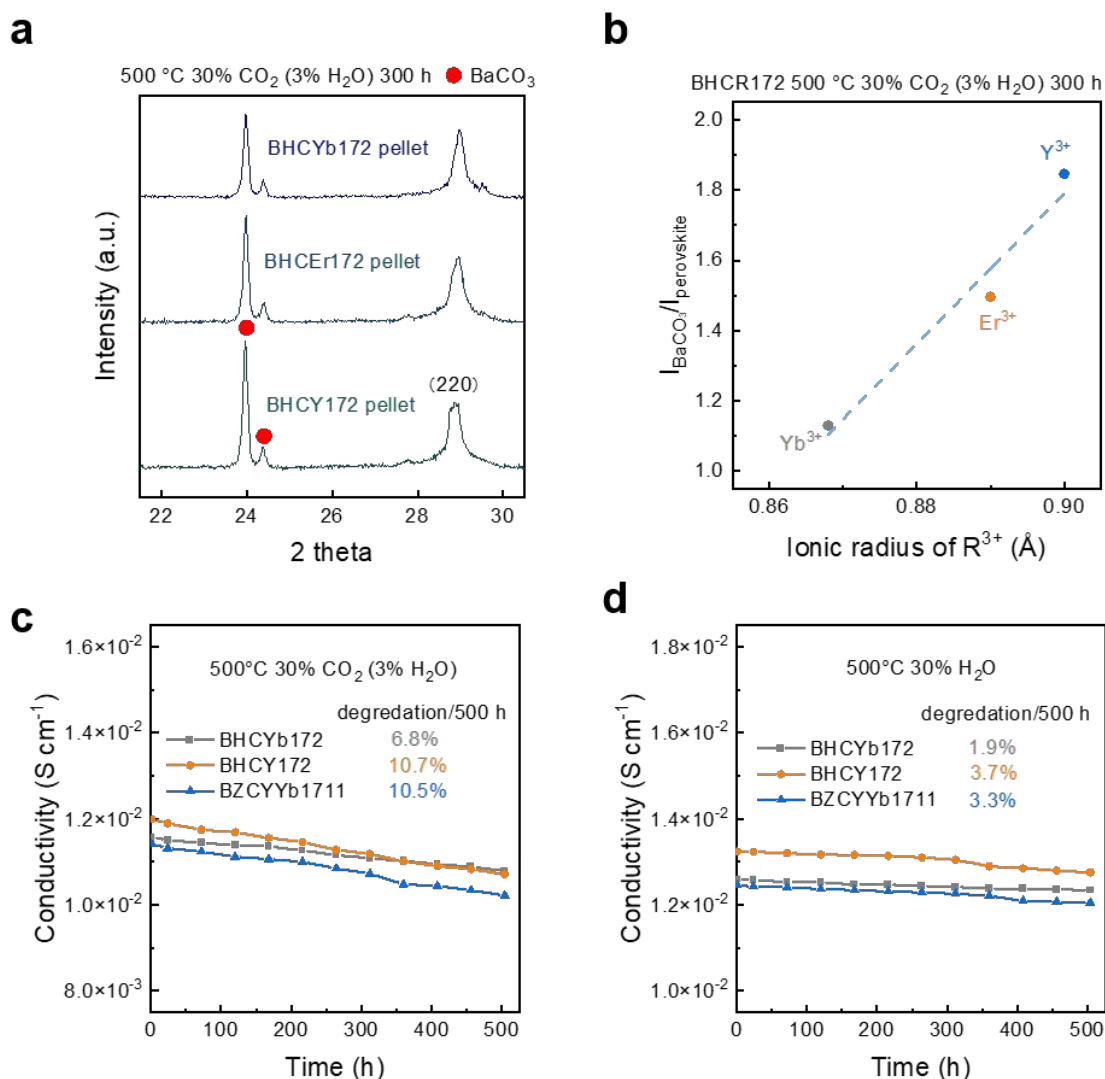

Fig. 4 a) Magnified view of XRD patterns of BHCR172 (R = Yb, Er, Y) pellets after exposure to 30% CO_2 and 3% H_2O in Ar at 500 °C for 300 h. b) Intensity ratio between the $BaCO_3$ and perovskite (220) peaks of BHCR172 as a function of ionic radius of R^{3+}. Conductivity of BHCYb172, BHCY172, and BZCYYb1711 over 500 h in c) 30% CO_2 and 3% H_2O, and d) 30% H_2O in Ar at 500 °C.

as shown in Fig. S7c (ESI). The results show that the correlation of the peak ratio with the dopant size is similar to that with conductivity in Fig. 3b. The data show that the conductivity and chemical stability of rare earth-doped barium cerate materials are closely related and a trade-off between them is difficult to avoid. In addition, the stability of the Yb-, Er-, and Y-doped materials were also evaluated by exposure to 30% CO_2 (3% H_2O) in Ar for 300 h at 500 °C. As shown in Fig. 4a and Fig. S8 (ESI), much more severe degradation was observed with a prolonged testing time. Similarly, Fig. 4b shows that the extent of degradation is strongly related to the dopant size. In the subsequent tests, BHCYb172 and $BaHf_{0.1}Ce_{0.7}Y_{0.2}O_{3-\delta}$ (BHCY172) were selected for further characterization and comparison since both Yb- and Y-doped materials showed desirable ionic transference numbers, and they are also the two constituents of the state-of-the-art proton conductor BZCYYb.

To understand the effect of degradation on the electrochemical performance of these materials, long-term conductivity evolution was measured in 30% CO_2 (3% H_2O) in Ar and 30% H_2O in Ar for 500 h at 500 °C (Fig. 4c-d). The %degradation/500h of BHCYb172 and BHCY172 upon CO_2 exposure is 6.8% and 10.7%, respectively, and 1.9% and 3.7% upon H_2O exposure, respectively. It is clear that the perovskite $Ba(Hf,Ce)O_3$-based proton conductors are more stable in high concentration of H_2O than CO_2. The results show that the degradation proceeds slowly over the 500 h for both BHCYb172 and BHCY172, while BHCYb172 exhibits a much lower percentage of conductivity degradation under both testing conditions over the entire 500 h, suggesting Yb-doping positively affects the stability of the electrolyte materials. Moreover, BZCYYb1711 was also included for comparison, and it is worth noting that with 10% Yb-doping, BZCYYb1711 shows similar degradation rate to that of BHCY172, which is likely because $BaZrO_3$ is less stable than $BaHfO_3$, and that effect compensates the substitution of 10% Y by Yb.

For thick pellet samples, it is possible that a thin layer of degradation phase may form at the surface initially, preventing further reaction between the contaminants and the bulk materials. As such, fine powders of BHCYb172 and BHCY172 were exposed to 10% CO_2 (3% H_2O) and Ar for 20 h at 500 °C for further verification. As shown in Fig. S9a-b (ESI), $BaCO_3$ was detected for both BHCYb172 and BHCY172, and the main $BaCO_3$ peak has a greater intensity for BHCY172 than for BHCYb172, confirming the better stability of BHCYb172. Again, the $BaCO_3$ peak intensity is comparable for BHCY172 and BZCYYb1711, implying that the two compounds have similar stability, which is consistent with the results from long-term conductivity measurements.

While stability measurements were performed using electrolyte pellets and powder samples, the actual solid oxide fuel cells (SOFCs) and solid oxide electrolysis cells (SOECs) for electrochemical performance evaluation were based on an electrolyte layer that is only tens of microns thick. Therefore, to verify the stability of these materials under more realistic SOFC/SOEC operating conditions, XRD patterns of the surface of the BHCYb172 and BHCY172-based fuel electrode-supported half cells were collected after exposure to 30% CO_2 (3% H_2O) in

Ar for 300 h at 500 °C. Here, the Yb-doped material also shows improved stability as compared to the Y-doped counterpart (Fig. S9c-d, ESI). Fig. S10 (ESI) shows the corresponding surface morphology after long-term CO_2 exposure. While the original electrolyte grain structures cannot be observed as the surfaces are heavily covered by $BaCO_3$, the BHCYb172-based cell shows a smaller $BaCO_3$ particle size on average as compared to the BHCY172-based cell.

DFT-based calculations

Along with experimental results, DFT-based calculations were used to study the stability of BHCR172 against H_2O and CO_2. Thermodynamic analysis in Fig. 5a-b shows that the Gibbs free energy (ΔG) of the reaction between BHCYb172 and H_2O is higher than that of the Er- and Y-doped electrolytes, indicating a higher H_2O tolerance due to Yb incorporation, which is consistent with the results from the stability measurements.

To emphasize the influence of rare earth dopants on the stability of electrolyte materials, the CO_2 and H_2O adsorption behaviors were investigated with AO-terminated BHCR172 (001) surfaces (Fig. 5c).[49-51] For Yb-, Er-, and Y-doped BHCR172, the calculated CO_2 chemical adsorption energies are -3.28, -3.37, and -3.51 eV, respectively, while the H_2O adsorption energies are -2.59, -2.67, and -2.76 eV, respectively (Fig. 5d). The DFT-based calculations further confirm the superiority of Yb-doping in suppressing surface CO_2 and H_2O adsorption. The calculated E_{ads} values show a clear trend with respect to dopant size for both the CO_2 and H_2O contamination cases, which is similar to the phenomenon observed in Fig. 4b and Fig. S7c (ESI).

Both experimental and computational results show that Yb-doping enhances the stability of electrolyte materials against both CO_2 and H_2O exposure more than other conventional trivalent dopants such as Er^{3+} and Y^{3+}. Specifically, the optimized composition, BHCYb172, showed sufficient chemical stability even under harsh conditions such as 30% H_2O at 500 °C (Fig. 4d). Furthermore, the comparable conductivity to that of the state-of-the-art BZCYYb1711 suggests that BHCYb172 could be a promising electrolyte candidate for SOFC and SOEC applications.

Compatibility with electrode materials

It is critical for electrolyte materials to be chemically compatible with both air and fuel electrode components during cell fabrication and operation, especially the high temperature co-firing processes. First, the chemical compatibility between BHCR172 and a highly active air electrode material $Ba_{0.9}Co_{0.7}Fe_{0.2}Nb_{0.1}O_{3-\delta}$ (BCFN) was investigated. Fig. S11 (ESI) shows the XRD patterns of the powder mixture of BHCR172 and BCFN (in a weight ratio of 1:1) after annealing at 1000 °C for 4 h. Both BHCR172 and BCFN maintained their initial phases, and no secondary peaks were observed.
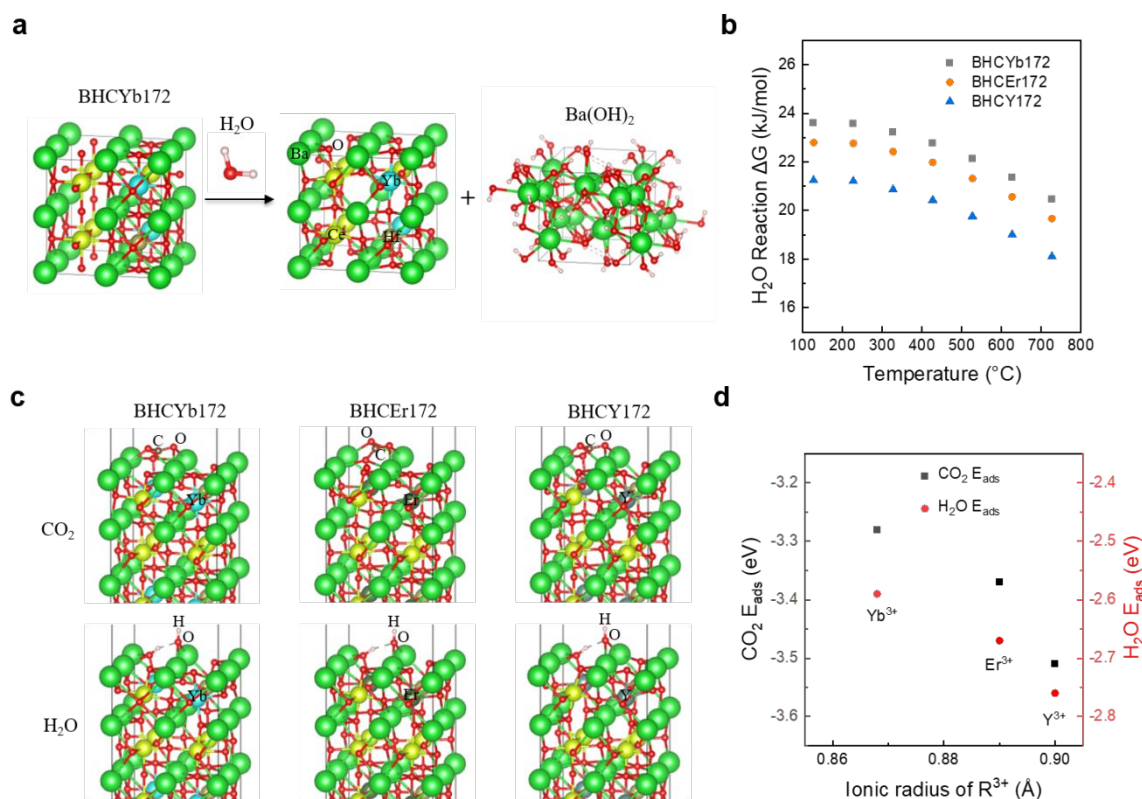
Fig. 5 a) The H_2O reaction schematic between BHCYb172 and H_2O. b) Gibbs free energy curves for the reaction of H_2O with BHCR172 (R=Yb, Er, Y). c) The CO_2 (top) and H_2O (bottom) adsorption behavior for AO-terminated BHCR172 (001) surfaces. d) CO_2 and H_2O E_{ads} as a function of the ionic radius of R^{3+}.

As the fuel electrode is often composed of an electrolyte-NiO cermet, the chemical compatibility between BHCR172 and NiO was examined. Unlike air electrode fabrication, the co-firing process for the fuel electrode-electrolyte bilayer takes place at much higher temperatures (>1400 °C), which easily induces reactions between cell components.[52] Fig. 6a and Fig. S12 (ESI) shows the XRD patterns of a mixture of BHCR172 and NiO (in a weight ratio of 1:1) after firing at 1400 °C for 5 h. For BHCYb172, no other peaks exist besides the perovskite peaks and NiO peaks. However, for the electrolytes doped with Er, Y, Gd, and Sm, the XRD patterns display the existence of small peaks associated with BaR_2NiO_5. Additionally, Fig. 6b shows that the relative intensity of the BaR_2NiO_5 peak displays strong correlation with the ionic radius of the dopant. It has been reported that the thermodynamic driving force for dopant segregation increases with increasing dopant size, especially at elevated temperatures where dopants are mobile, which could lead to the reaction between NiO and segregated cations.[53, 54] Fig. S13a-e (ESI) shows that BaR_2NiO_5 starts to form at temperatures as low as 1100 °C, so a lower sintering temperature may not be able to completely diminish the formation of this phase. At a co-firing temperature of 1100 °C, larger shrinkage of the pellet was found for those materials that exhibited a strong reaction with NiO (Fig. S13f, ESI). The formation of BaR_2NiO_5 is known to promote sintering of electrolyte materials as an intermediate liquid phase, thus stronger interaction with NiO is possibly contributing to an enhanced sintering ability for those samples doped with larger trivalent dopants.[55-58]

To further confirm the reactivity under cell fabrication processes, fuel electrode-supported half cells using BHCYb172 and BHCY172 electrolytes were fabricated and characterized after co-firing. Fig. 6c-d shows the SEM images of the electrolyte surface of the two cells, and the formation of secondary particles can be clearly identified on the BHCY172-based half cell, while the BHCYb172-based cell exhibits a clear and smooth surface. Further energy-dispersive X-ray spectroscopy (EDS) elemental mapping analysis shows that the secondary particles are rich in Y and Ni while the presence of Hf and Ce is not detected, which matches the elemental constituents of BaY_2NiO_5 (Fig. 6e-f and Fig. S14, ESI). Unlike pellet fabrication where NiO is added as a sintering aid, the only NiO source during cell fabrication is from the fuel electrode, indicating diffusion of NiO at high temperatures is extensive enough to penetrate the thickness of the electrolyte layer, which is around 10 μm. As shown in Fig. S15-16 (ESI), a BHCY172-based half cell with a 50 μm thick electrolyte layer was fabricated, and the formation of BaY_2NiO_5 was still confirmed by both XRD and EDS after sintering, suggesting the diffusion length of NiO can be as far as 50 μm at elevated temperatures, and it is very difficult to suppress with conventional cell fabrication methods. In comparison, the cross-section of the BHCYb172-based cell is free of secondary particles, suggesting an excellent phase compatibility between Yb-doped electrolytes and NiO (Fig. S17, ESI).

It is reported that the reactivity between the electrolyte and NiO depends sensitively on the doping concentration of R^{3+}. For example, the solubility of Y in the Ba-Zr-Y-Ni system at
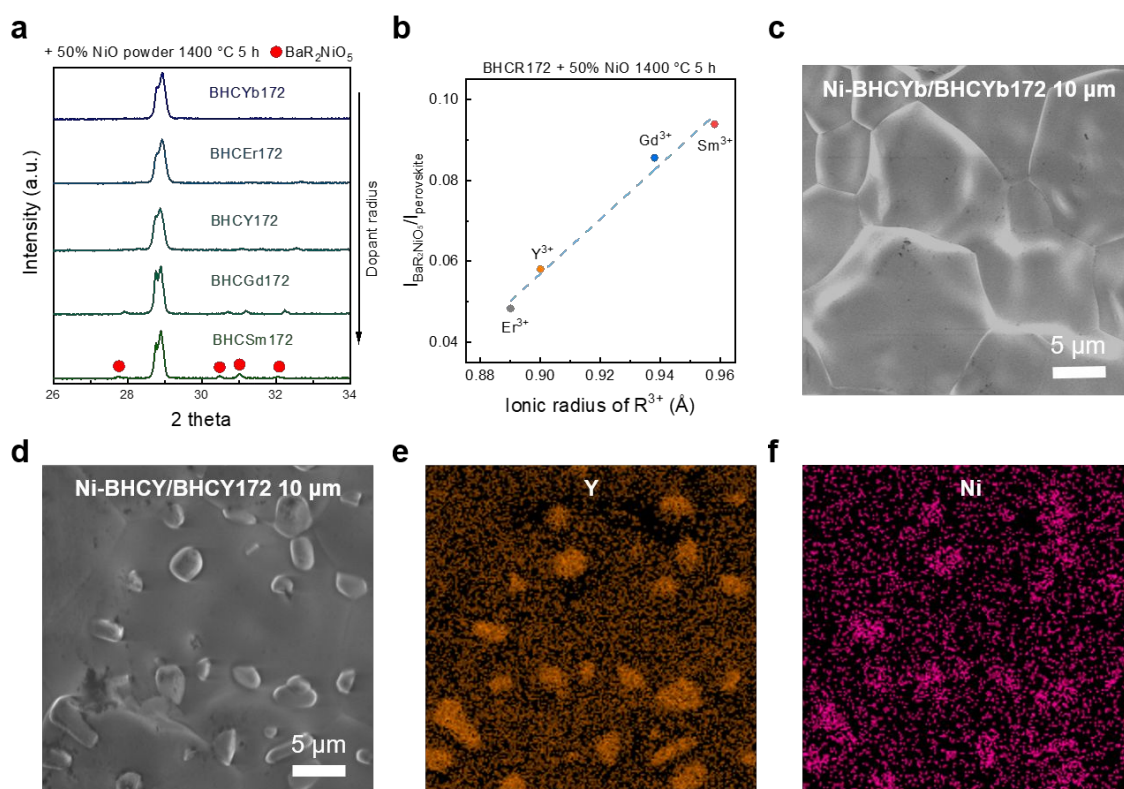
Fig. 6 a) Magnified view of XRD patterns of BHCR172 (R = Yb, Er, Y, Gd, Sm) after firing with NiO at 1400 °C for 5 h. b) Intensity ratio between the BaR_2NiO_5 and perovskite (220) peaks of BHCR172 (R = Er, Y, Gd, Sm) as a function of the ionic radius of R^{3+}. c) SEM image of the electrolyte surface of a Ni-BHCYb/BHCYb172 half cell with an electrolyte thickness of 10 μm after firing at 1400 °C for 5 h. d-f) SEM image and EDS mapping of the electrolyte surface of a Ni-BHCY/BHCY172 half cell with an electrolyte thickness of 10 μm after firing at 1400 °C for 5 h.

temperatures above 1500 °C is about 12%, and the solubility of larger dopants such as Gd and Sm could be even lower.[59] As confirmed in Fig. S18 (ESI), $BaHf_{0.1}Ce_{0.8}Y_{0.1}O_{3-\delta}$ (BHCY181) shows no compatibility issues with NiO, and BHCYb starts to react with NiO when the Yb content is increased to 30% on the B-site, suggesting the solubility limit of Yb in the Ba-Hf-Ce-Yb-Ni system is between 20 and 30% at elevated temperatures. Although the compatibility issue can be resolved with lower Y content, it is found that the conductivity of BHCY181 is significantly lower than that of BHCY172, due likely to the lack of oxygen vacancies available for proton incorporation at such a low doping level (Fig. S19, ESI). It is also found that the conductivity of $BaHf_{0.1}Ce_{0.6}Yb_{0.3}O_{3-\delta}$ (BHCYb163) is comparable to that of BHCYb172, but 20% Yb^{3+} doping on the B-site is indeed the optimal concentration to have both good conductivity and chemical compatibility with NiO.[60, 61]

It is possible that trivalent dopants with even smaller ionic radii, such as In^{3+}, may have better compatibility during cell fabrication. However, it is reported that In-doped electrolytes give poor conductivity, which leaves Yb the most practical acceptor dopant that shows excellent compatibility with NiO at a doping concentration of 20% on the B-site, while maintaining adequate conductivity.[35, 62]

In addition, our results may explain why the state-of-the-art BZCYYb1711 electrolyte gives excellent cell performance.[63, 64] First, although the total doping level on the B-site is 20%, the Y content is only 10%, which is lower than the solubility limit

during co-firing. As a result, BZCYYb1711 shows excellent compatibility with NiO and the formation of secondary phases is prevented (Fig. S20, ESI). In addition, Yb- and Y-doping are responsible for maintaining high stability and conductivity, respectively, as confirmed by our results. Furthermore, the NiO compatibility of two other commonly used proton-conducting electrolytes, $BaZr_{0.4}Ce_{0.4}Y_{0.1}Yb_{0.1}O_{3-\delta}$ (BZCYYb4411) and $BaZr_{0.8}Y_{0.2}O_{3-\delta}$ (BZY82) were also investigated. While BZCYYb4411 shows no reaction, the formation of BaY_2NiO_5 phase can be clearly identified with BZY82, further confirming Y-doping beyond 10% on the B-site may cause NiO compatibility issues during cell fabrication (Fig. S21, ESI). It is interesting to note that the degree of reaction between BZY82 and NiO is more severe than the case of BHCY172, indicating the other constituents in the electrolyte composition might also have some impact on NiO reactivity. Accordingly, doping with multiple cations on the B-site for different functionalities could be a viable strategy to achieve balanced NiO compatibility and electrochemical performance during electrolyte development.

Electrochemical performance of fuel electrode-supported single cells

NiO is widely used as a sintering aid for electrolyte densification due to the formation of a liquid BaR_2NiO_5 phase during sintering. However, this phase may not completely disappear after cell fabrication if the doping concentration of R^{3+} exceeds the solubility limit in the Ba-Hf/Ce/Zr-R-Ni system. Formation of this
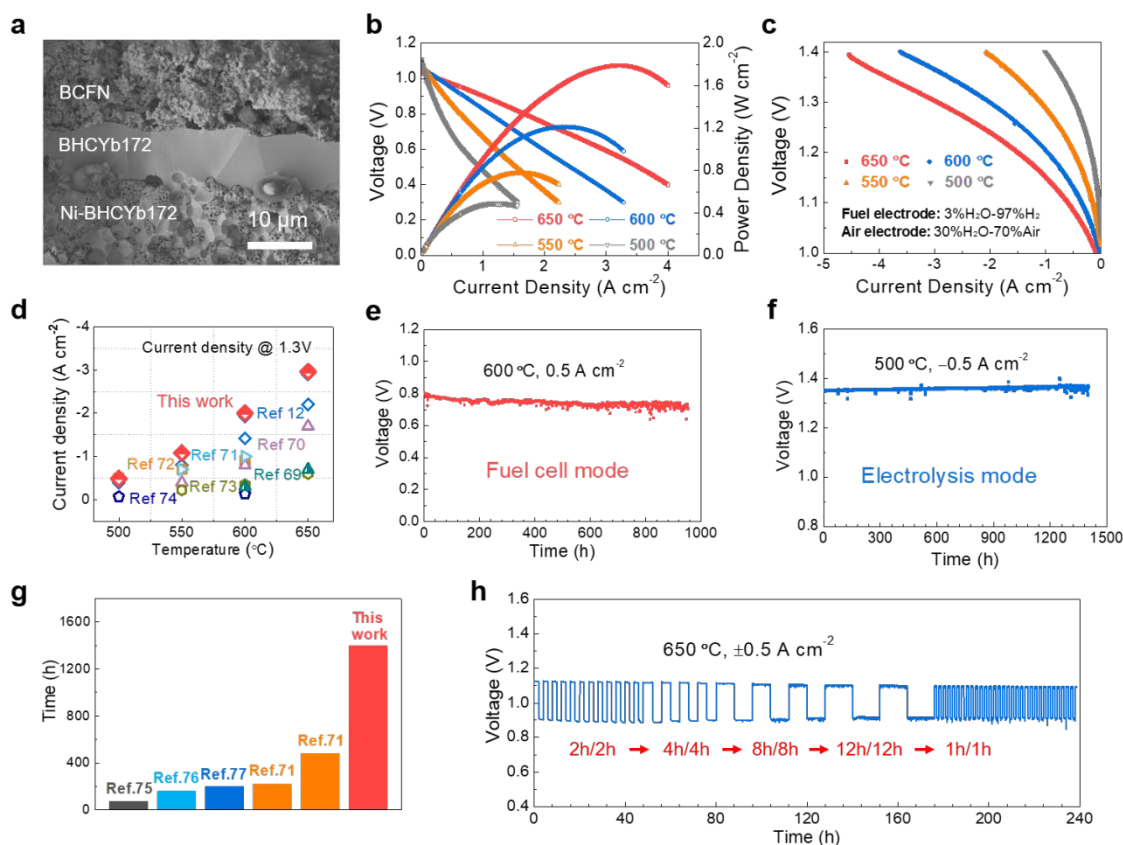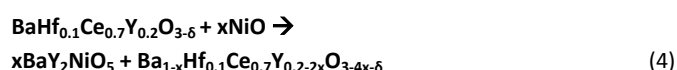
Fig. 7 a) Cross-sectional SEM image of the Ni-BHCYb172/BHCYb172/BCFN single cell. b) Typical I-V-P curves measured in the fuel cell mode at 500-650 °C with H_2 (3% H_2O) in the fuel electrode and ambient air in the air electrode. c) Typical I-V curves measured in the electrolysis mode at 500-650 °C with H_2 (3% H_2O) in the fuel electrode and air (30% H_2O) in the air electrode. d) Comparison of current density at 1.3V of SOECs based on proton conductors at 500-650 °C.[12, 69-74] e) Long-term stability in the fuel cell mode with H_2 (3% H_2O) in the fuel electrode and ambient air in the air electrode at 0.5 A cm^{-2} and 600 °C. f) Long-term stability in the electrolysis mode with H_2 (3% H_2O) in the fuel electrode and air (3% H_2O) in the air electrode at -0.5 A cm^{-2} and 500 °C. g) Comparison of the duration of stability tests of proton-conducting electrolysis cells at 500 °C.[71, 75-77] h) Reversible operation of the cell: the cell voltage as a function of time when the operating mode was switched between the fuel cell and electrolysis modes (2-12 h for each mode) at a current density of ±0.5 A cm^{-2} at 650 °C.

phase will lead to exsolution of Ba and Y from the bulk electrolyte phase, resulting in deviation from the desired electrolyte composition and electrochemical properties (Reaction 4).[65-67] Also, the existence of these secondary particles on the electrolyte surface might create a poor interface between the electrolyte and air electrode, leading to an enlarged polarization resistance. Moreover, BaR_2NiO_5 is more electronically conducting than the parent electrolyte phase, thus the formation of this phase might result in increased electronic leakage through the electrolyte layer. Furthermore, the difference in thermal expansion coefficient between BaR_2NiO_5 and the electrolyte phase might cause cracking in the electrolyte layer during thermal cycling, causing other problems (e.g., gas leakage).[68] To test these hypotheses, single cells with a configuration of Ni-BHCYb172/BHCYb172/BCFN and Ni-BHCY172/BHCY172/BCFN were constructed to evaluate the cell performance. As shown in Fig. 7a and Fig. S22 (ESI), dense electrolyte membranes with a thickness of about 10 μm were achieved in both cases. The open circuit voltages (OCVs) of the BHCYb172-based cell are 1.09, 1.07, and 1.04 at 550, 600, and 650 °C, respectively, and the peak power densities (PPDs) are 0.77, 1.21, and 1.79 W cm^{-2} at 550, 600, and 650 °C, respectively, as shown in Fig. 7b. Further,

another cell was tested to show the effect of feed gas in the air electrode on the cell performance (Fig. S23, ESI). When the oxidant was switched from ambient air to pure O_2, the PPDs of the fuel cell increased from 0.84 to 1.18 W cm^{-2} at 550 °C and from 1.33 to 1.74 W cm^{-2} at 600 °C. The increase in power output is attributed to both the Nernst effect (higher open cell voltage) and enhanced mass transfer of oxygen to the active sites (lower resistance to oxygen transport). The performance achieved in the fuel cell mode is among the highest of those reported for proton-conducting solid oxide fuel cells (Table. S1, ESI). When compared to the OCVs and PPDs of the BHCY172-based cell, the BHCYb172-based cell shows substantial enhancement, which is consistent with our previous hypotheses (Fig. S24-25, ESI). Specifically, PPDs are boosted by about one-fold at all testing temperatures by using BHCYb172 rather than BHCY172. As shown in Fig. S26-27 (ESI), the BHCYb172-based cell exhibits both higher ohmic resistance (R_o) and polarization resistance (R_p) at all temperatures, due likely to the formation of BaY_2NiO_5 secondary particles, leading to lower cell performance. Thus, although the BHCY172 electrolyte offers higher conductivity than that of the Yb-doped counterpart, its performance cannot be fully realized in single cells due to poor chemical compatibility with NiO, and the same is also expected

for other electrolytes (such as BHCGd172) with poor NiO compatibility.

As shown in the long-term conductivity test of the electrolytes under exposure to 30% steam, the BHCYb172 electrolyte exhibits the best stability under realistic electrolysis operating conditions (Fig. 4d). As such, BHCYb172 was also tested as an electrolyte for water electrolysis. Fig. 7c shows the current-voltage curves of the electrolysis cell when the fuel electrode was exposed to humidified hydrogen (with 3% H_2O) and the air electrode was exposed to humidified air (30% H_2O). As is well known, cell performance depends sensitively on the composition of the feed gas to the fuel electrode (Fig. S28, ESI). In this study, H_2 (3% H_2O) was supplied to the fuel electrode in order to compare the cell performance with those reported in literature under similar conditions.[12, 69] At 600 ℃, a current density of 2.0 A cm^{-2} at a cell voltage of 1.3 V was obtained, which is one of the best performances ever reported in literature (Fig. 7d).[12, 69-74] Faradaic efficiencies are shown in Fig. S29 (ESI). The roundtrip electric effeciency (defined as the ratio of the cell voltage under the fuel cell mode at 0.5 A cm^{-2} to the cell voltage under the electrolysis mode at 1 A cm^{-2}) of the reversible cell was about 84% at 650 ℃ and 79% at 600 ℃. As shown in Fig. 7e-f, remarkable long-term durability of the cell in both fuel cell and electrolysis modes were demonstrated. Especially, for the electrolysis cell, only 0.8% degradation/1000h was observed for a total testing time over 1400 h, which is among the best stability reported, especially at such a low testing temperature for proton conductor-based cells (Fig. 7g).[71, 75-77] It is noted that the degradatioin rate of the cell operated in the electrolysis mode (about 0.8%/1000h, Fig. 7f) is smaller than that of the fuel cell mode (about 9%/1000 h, Fig. 7e), attributed likely to the degradation of the air electrode-electrolyte interface due to water generation, charge transfer, and oxygen transport processes in the fuel cell mode.[78] Cross-sectional SEM images of the BHCYb172 cell after the 1400 h durability test is shown in Fig. S30 (ESI), revealing a dense electrolyte membrane and good bonding with the two porous electrodes. In addition, the durability of the cells was also tested under aggressive electrolysis conditions; the air electrode was exposed to wet air with 30% and 50% H_2O. As shown in Fig. S31 (ESI), excellent long-term stability of the cells was demonstrated at a current density of -1 A cm^{-2} at 600 ℃ for over 200 h for both conditions. Furthermore, the reversibility of the cell was evaluated at 650 ℃ by cyclic operation between the fuel cell mode and the electrolysis mode at a current density of ±0.5 A cm^{-2}, and there was minimal degradation for over 200 h and 50 cycles (Fig. 7h).

$$BaHf_{0.1}Ce_{0.7}Y_{0.2}O_{3-\delta} + xNiO \rightarrow$$
$$xBaY_2NiO_5 + Ba_{1-x}Hf_{0.1}Ce_{0.7}Y_{0.2-2x}O_{3-4x-\delta} \qquad (4)$$

Conclusions

We have successfully developed a Yb-doped barium hafnate-cerate proton-conducting electrolyte, $BaHf_{0.1}Ce_{0.7}Yb_{0.2}O_{3-\delta}$, which demonstrates high ionic conductivity, excellent chemical stability against steam and CO_2, adequate compatibility with NiO during co-sintering and cell fabrication, and exceptional cell performance in both the fuel cell and the electrolysis modes. In particular, the strong correlation of the size of the B-site trivalent dopant with the electrical conductivity, chemical stability, and NiO compatibility confirmed that the selection of proper B-site dopant is critical to cell performance, as evidenced by both experimental and DFT-based computational results. Single cells based on BHCYb172 achieved significantly higher performance with excellent durability when compared to the Y-doped counterpart (BHCY172), although the latter displays higher ionic conductivity. The poor cell performance is attributed to the formation of a secondary phase, BaY_2NiO_5, during cell fabrication, as confirmed by XRD, EDS, and electrochemical measurements. Further, the BHCYb172-based cells delivered an extraordinary peak power density of 1.33 (or 1.74) W cm^{-2} at 600 ℃ when air (or oxygen) was used as oxidant in the fuel cell mode and a high current density of 2.0 A cm^{-2} at a cell voltage of 1.3 V at 600 ℃ in the electrolysis mode while maintaining excellent durability for more than 1000 h. These performances are among the best ever reported for reversible solid oxide cells under similar operating conditions. These results may provide insights into rational selection of dopants for the design of proton-conducting electrolytes for high-performance solid oxide cells.

Author Contributions

Z.L. and Y.Z. contributed equally to this work. M.L., Y.Z., and Y.L. conceived the project and supervised the research. Z.L. synthesized, tested, and characterized the electrolyte materials. Y.Z. fabricated and tested single cells. X.H. performed computational studies and analysed the computational data. N.K., T.L, and Y.D characterized the materials and cells by EDS, XRD, and TEM. W.Z. synthesized air electrode materials. Z.L. tested single cells. All the authors discussed the results. Z.L. wrote the manuscript with input from all the authors. Y.Z., N.K., and M.L. revised the manuscript.

Conflicts of interest

There are no conflicts to declare.

Acknowledgements

Notes and references

1. A. Evans, V. Strezov and T. J. Evans, *Renew Sust Energ Rev*, 2012, **16**, 4141-4147.
2. B. Coelho, A. C. Oliveira and A. Mendes, *Energ Environ Sci*, 2010, **3**, 1398-1405.
3. L. Malavasi, C. A. J. Fisher and M. S. Islam, *Chem Soc Rev*, 2010, **39**, 4370-4387.
4. J. Kim, S. Sengodan, S. Kim, O. Kwon, Y. Bu and G. Kim, *Renew Sust Energ Rev*, 2019, **109**, 606-618.
5. L. Bi, S. Boulfrad and E. Traversa, *Chem Soc Rev*, 2014, **43**, 8255-8270.
6. L. B. Lei, J. H. Zhang, Z. H. Yuan, J. P. Liu, M. Ni and F. L. Chen, *Adv Funct Mater*, 2019, **29**.
7. W. Wang, D. Medvedev and Z. P. Shao, *Adv Funct Mater*, 2018, **28**.
8. E. Fabbri, D. Pergolesi and E. Traversa, *Chem Soc Rev*, 2010, **39**, 4355-4369.
9. K. H. Ryu and S. M. Haile, *Solid State Ionics*, 1999, **125**, 355-367.
10. C. D. Zuo, S. E. Dorris, U. Balachandran and M. L. Liu, *Chem Mater*, 2006, **18**, 4647-4650.
11. K. Bae, D. Y. Jang, H. J. Choi, D. Kim, J. Hong, B. K. Kim, J. H. Lee, J. W. Son and J. H. Shim, *Nat Commun*, 2017, **8**.
12. S. Choi, T. C. Davenport and S. M. Haile, *Energ Environ Sci*, 2019, **12**, 206-215.
13. H. An, H. W. Lee, B. K. Kim, J. W. Son, K. J. Yoon, H. Kim, D. Shin, H. I. Ji and J. H. Lee, *Nat Energy*, 2018, **3**, 870-875.
14. Y. Chen, B. deGlee, Y. Tang, Z. Y. Wang, B. T. Zhao, Y. C. Wei, L. Zhang, S. Yoo, K. Pei, J. H. Kim, Y. Ding, P. Hu, F. F. Tao and M. L. Liu, *Nat Energy*, 2018, **3**, 1042-1050.
15. L. Bi, S. P. Shafi and E. Traversa, *J Mater Chem A*, 2015, **3**, 5815-5819.
16. D. Medvedev, A. Murashkina, E. Pikalova, A. Demin, A. Podias and P. Tsiakaras, *Prog Mater Sci*, 2014, **60**, 72-129.
17. D. L. Han, X. Liu, T. S. Bjorheim and T. Uda, *Adv Energy Mater*, 2021, **11**.
18. A. Trivino-Pelaez, D. Perez-Coll, M. Aparicio, D. P. Fagg, J. Mosa and G. C. Mather, *J Mater Chem A*, 2022, DOI: 10.1039/d1ta09998a.
19. Y. Yamazaki, R. Hernandez-Sanchez and S. M. Haile, *Chem Mater*, 2009, **21**, 2755-2762.
20. Y. Yoo and N. Lim, *J Power Sources*, 2013, **229**, 48-57.
21. S. Ricote, N. Bonanos and G. Caboche, *Solid State Ionics*, 2009, **180**, 990-997.
22. K. D. Kreuer, *Annu Rev Mater Res*, 2003, **33**, 333-359.
23. K. D. Kreuer, *Solid State Ionics*, 1999, **125**, 285-302.
24. M. Cherry, M. S. Islam, J. D. Gale and C. R. A. Catlow, *Solid State Ionics*, 1995, **77**, 207-209.
25. L. He, F. Zhang, Y. Xuan, L. Zhang, H. Y. Gao, H. Q. Pan, S. Lian, M. Y. Wang, J. K. Yin, X. Chen, J. F. Ren and M. N. Chen, *J Electrochem Soc*, 2021, **168**.
26. Y. Yamazaki, F. Blanc, Y. Okuyama, L. Buannic, J. C. Lucio-Vega, C. P. Grey and S. M. Haile, *Nat Mater*, 2013, **12**, 647-651.
27. H. S. Kim, A. Jang, S. Y. Choi, W. Jung and S. Y. Chung, *Angew Chem Int Edit*, 2016, **55**, 13499-13503.
28. H. Matsumoto, Y. Kawasaki, N. Ito, M. Enoki and T. Ishihara, *Electrochem Solid St*, 2007, **10**, B77-B80.
29. S. M. Haile, G. Staneff and K. H. Ryu, *J Mater Sci*, 2001, **36**, 1149-1160.
30. R. Murphy, Y. C. Zhou, L. Zhang, L. Soule, W. L. Zhang, Y. Chen and M. L. Liu, *Adv Funct Mater*, 2020, **30**.
31. S. W. Wang, Y. Chen, S. M. Fang, L. L. Zhang, M. Tang, K. An, K. S. Brinkman and F. L. Chen, *Chem Mater*, 2014, **26**, 2021-2029.
32. F. M. Draber, C. Ader, J. P. Arnold, S. Eisele, S. Grieshammer, S. Yamaguchi and M. Martin, *Nat Mater*, 2020, **19**, 577-577.
33. M. S. Islam, S. Wang, A. M. Nolan and Y. F. Mo, *Chem Mater*, 2021, **33**, 8278-8288.
34. L. Yang, S. Z. Wang, K. Blinn, M. F. Liu, Z. Liu, Z. Cheng and M. L. Liu, *Science*, 2009, **326**, 126-129.
35. M. Amsif, D. Marrero-Lopez, J. C. Ruiz-Morales, S. N. Savvin, M. Gabas and P. Nunez, *J Power Sources*, 2011, **196**, 3461-3469.
36. E. Gilardi, E. Fabbri, L. Bi, J. L. M. Rupp, T. Lippert, D. Pergolesi and E. Traversa, *J Phys Chem C*, 2017, **121**, 9739-9747.
37. J. Guan, S. E. Dorris, U. Balachandran and M. Liu, *Solid State Ionics*, 1997, **100**, 45-52.
38. Y. C. Zhou, E. Z. Liu, Y. Chen, Y. C. Liu, L. Zhang, W. L. Zhang, Z. Y. Luo, N. Kane, B. Zhao, L. Soule, Y. H. Niu, Y. Ding, H. P. Ding, D. Ding and M. L. Liu, *Acs Energy Lett*, 2021, **6**, 1511-1520.
39. H. Y. Zhu, S. Ricote, C. C. Duan, R. P. O'Hayre and R. J. Kee, *J Electrochem Soc*, 2018, **165**, F845-F853.
40. K. Nomura and H. Kageyama, *Solid State Ionics*, 2007, **178**, 661-665.
41. I. Zvonareva, X. Z. Fu, D. Medvedev and Z. P. Shao, *Energ Environ Sci*, 2022, **15**, 439-465.
42. C. C. Duan, J. K. Huang, N. Sullivan and R. O'Hayre, *Appl Phys Rev*, 2020, **7**.
43. I. H. Kim, D. K. Lim, H. Bae, A. Bhardwaj, J. Y. Park and S. J. Song, *J Mater Chem A*, 2019, **7**, 21321-21328.
44. H. Iwahara, T. Yajima and H. Ushida, *Solid State Ionics*, 1994, **70**, 267-271.
45. S. Choi, C. J. Kucharczyk, Y. G. Liang, X. H. Zhang, I. Takeuchi, H. I. Ji and S. M. Haile, *Nat Energy*, 2018, **3**, 202-210.
46. S. V. Bhide and A. V. Virkar, *J Electrochem Soc*, 1999, **146**, 2038-2044.
47. C. W. Tanner and A. V. Virkar, *J Electrochem Soc*, 1996, **143**, 1386-1389.
48. E. Fabbri, A. D'Epifanio, E. Di Bartolomeo, S. Licoccia and E. Traversa, *Solid State Ionics*, 2008, **179**, 558-564.
49. R. Sazinas, M. F. Sunding, A. Thogersen, I. Sakaguchi, T. Norby, T. Grande and J. M. Polfus, *J Mater Chem A*, 2019, **7**, 3848-3856.
50. J. M. Polfus, J. Yang and B. Yildiz, *J Mater Chem A*, 2018, **6**, 24823-24830.
51. X. Y. Hu, Y. Xie, Y. H. Wan, Y. Yang, X. J. Wu and C. R. Xia, *Appl Catal B-Environ*, 2021, **286**.
52. Y. M. Guo, R. Ran and Z. P. Shao, *Int J Hydrogen Energ*, 2011, **36**, 1683-1691.
53. A. Lindman, T. S. Bjorheim and G. Wahnstrom, *J Mater Chem A*, 2017, **5**, 13421-13429.
54. S. Imashuku, T. Uda, Y. Nose, G. Taniguchi, Y. Ito and Y. Awakura, *J Electrochem Soc*, 2009, **156**, B1-B8.
55. Y. Liu, L. Yang, M. F. Liu, Z. Y. Tang and M. L. Liu, *J Power Sources*, 2011, **196**, 9980-9984.
56. J. H. Tong, D. Clark, L. Bernau, M. Sanders and R. O'Hayre, *J Mater Chem*, 2010, **20**, 6333-6341.
57. Y. Y. Huang, R. Merkle and J. Maier, *J Mater Chem A*, 2021, **9**, 14775-14785.

58. J. H. Tong, D. Clark, L. Bernau, A. Subramaniyan and R. O'Hayre, *Solid State Ionics*, 2010, **181**, 1486-1498.
59. K. Ueno, N. Hatada, D. L. Han and T. Uda, *J Mater Chem A*, 2019, **7**, 7232-7241.
60. D. L. Han and T. Uda, *J Mater Chem A*, 2018, **6**, 18571-18582.
61. S. Kasamatsu, O. Sugino, T. Ogawa and A. Kuwabara, *J Mater Chem A*, 2020, **8**, 12674-12686.
62. T. Kuroha, Y. Niina, M. Shudo, G. Sakai, N. Matsunaga, T. Goto, K. Yamauchi, Y. Mikami and Y. Okuyama, *J Power Sources*, 2021, **506**.
63. C. C. Duan, J. H. Tong, M. Shang, S. Nikodemski, M. Sanders, S. Ricote, A. Almansoori and R. O'Hayre, *Science*, 2015, **349**, 1321-1326.
64. C. C. Duan, R. J. Kee, H. Y. Zhu, C. Karakaya, Y. C. Chen, S. Ricote, A. Jarry, E. J. Crumlin, D. Hook, R. Braun, N. P. Sullivan and R. O'Hayre, *Nature*, 2018, **557**, 217-+.
65. M. Choi, J. Paik, D. Kim, D. Woo, J. Lee, S. J. Kim, J. Lee and W. Lee, *Energ Environ Sci*, 2021, **14**, 6476-6483.
66. S. M. Fang, S. W. Wang, K. S. Brinkman, Q. Su, H. Y. Wang and F. L. Chen, *J Power Sources*, 2015, **278**, 614-622.
67. H. S. Kim, H. B. Bae, W. Jung and S. Y. Chung, *Nano Lett*, 2018, **18**, 1110-1117.
68. D. L. Han, J. Iihara, S. Uemura, K. Kazumi, C. Hiraiwa, M. Majima and T. Uda, *J Mater Chem A*, 2016, **4**, 10601-10608.
69. D. M. Huan, N. Shi, L. Zhang, W. Z. Tan, W. H. Wang, C. R. Xia, R. R. Peng and Y. L. Lu, *Acs Appl Mater Inter*, 2018, **10**, 1761-1770.
70. J. Kim, A. Jun, O. Gwon, S. Yoo, M. Liu, J. Shin, T. H. Lim and G. Kim, *Nano Energy*, 2018, **44**, 121-126.
71. H. P. Ding, W. Wu, C. Jiang, Y. Ding, W. J. Bian, B. X. Hu, P. Singh, C. J. Orme, L. C. Wang, Y. Y. Zhang and D. Ding, *Nat Commun*, 2020, **11**.
72. C. C. Duan, R. Kee, H. Y. Zhu, N. Sullivan, L. Z. Zhu, L. Z. Bian, D. Jennings and R. O'Hayre, *Nat Energy*, 2019, **4**, 230-240.
73. W. Y. Li, B. Guan, L. Ma, S. S. Hu, N. Zhang and X. B. Liu, *J Mater Chem A*, 2018, **6**, 18057-18066.
74. E. Vollestad, R. Strandbakke, M. Tarach, D. Catalan-Martinez, M. L. Fontaine, D. Beeaff, D. R. Clark, J. M. Serra and T. Norby, *Nat Mater*, 2019, **18**, 752-+.
75. W. Wu, H. P. Ding, Y. Y. Zhang, Y. Ding, P. Katiyar, P. K. Majumdar, T. He and D. Ding, *Adv Sci*, 2018, **5**.
76. W. Tang, H. P. Ding, W. J. Bian, W. Wu, W. Y. Li, X. B. Liu, J. Y. Gomez, C. Y. R. Vera, M. Zhou and D. Ding, *J Mater Chem A*, 2020, **8**, 14600-14608.
77. Y. C. Zhou, W. L. Zhang, N. Kane, Z. Y. Luo, K. Pei, K. Sasaki, Y. M. Choi, Y. Chen, D. Ding and M. L. Liu, *Adv Funct Mater*, 2021, **31**.
78. L. Q. Le, C. H. Hernandez, M. H. Rodriguez, L. Z. Zhu, C. C. Duan, H. P. Ding, R. P. O'Hayre and N. P. Sullivan, *J Power Sources*, 2021, **482**.